Accepted Manuscript

# Nanosecond-laser conditioning of multilayer dielectric gratings for picosecond-petawatt laser systems

**Kun Shuai [1,2,3], Yuanan Zhao [1,2,3,10], Xiaofeng Liu [1,2,3,11], Xiangkun Lin [1,2,3], Zhilin Xia [4], Keqiang Qiu [5], Dawei Li [1,3], He Gong [1,6], Yan Zhou [1,6], Jian Sun [1,3], Li Zhou [7], Youen Jiang [7], Yaping Dai [8], Jianda Shao [1,3,9]**

[1] *Laboratory of Thin Film Optics, Shanghai Institute of Optics and Fine Mechanics, Shanghai 201800, China*

[2] *Center of Materials Science and Optoelectronics Engineering, University of Chinese Academy of Sciences, Beijing 100049, China*

[3] *Key Laboratory of Materials for High Power Laser, Chinese Academy of Sciences, Shanghai 201800, China*

[4] *School of Materials Science and Engineering, Wuhan University of Technology, Wuhan, Hubei 430070, China*

[5] *National Synchrotron Radiation Laboratory, University of Science and Technology of China, Hefei, Anhui 230029, China*

[6] *School of Optical-Electrical and Computer Engineering, University of Shanghai for Science and Technology, Shanghai 200093, China*

[7] *National Laboratory on High Power Laser and Physics, Shanghai Institute of Optics and Fine Mechanics, CAS, Shanghai, 201800, China*

[8] *Research Center of Laser Fusion, China Academy of Engineering Physics, Mianyang, Sichuan 621900, China*

[9] *Hangzhou Institute for Advanced Study, University of Chinese Academy of Sciences, Hangzhou 310024, China*

[10] *yazhao@siom.ac.cn*

[11] *liuxiaofeng@siom.ac.cn*

**Abstract** Multilayer dielectric gratings (MLDGs) are crucial for pulse compression in picosecond-petawatt laser systems. Bulged nodular defects, embedded in coating stacks during multilayer deposition, influence the lithographic process and performance of the final



10.1017/hpl.2023.74

MLDG products. In this study, the integration of nanosecond laser conditioning (NLC) into different manufacturing stages of MLDG was proposed for the first time: on multilayer dielectric films (MLDFs) and final grating products to improve laser-induced damage performance. The results suggest that the remaining nodular ejection pits introduced by the two protocols exhibit a high nanosecond-laser damage resistance, which remains stable when the irradiated laser fluence is more than twice the nanosecond-laser-induced damage threshold (nanosecond-LIDT) of the unconditioned MLDGs. Furthermore, the picosecond-LIDT of the nodular ejection pit conditioned on the MLDFs was ~40 % higher than that of the nodular defects, and the loss of the grating structure surrounding the nodular defects was avoided. Therefore, NLC is an effective strategy for improving the laser damage resistance of MLDGs.

***Key words:*** *Multilayer dielectric gratings; nanosecond laser conditioning; nodular defects; laser-induced damage threshold; picosecond-petawatt laser systems*

---

Correspondence to: Yuan'an Zhao, Laboratory of Thin Film Optics, Shanghai Institute of Optics and Fine Mechanics, Shanghai 201800, China. Email: yazhao@siom.ac.cn
Xiaofeng Liu, Laboratory of Thin Film Optics, Shanghai Institute of Optics and Fine Mechanics, Shanghai 201800, China. Email: liuxiaofeng@siom.ac.cn

# I. Introduction

High-energy petawatt laser systems (HPLSs) [1-4] have unparalleled application in inertial confinement fusion [5], laboratory extreme physics research [6], and laser-accelerated particle beams [7,8]. Chirped pulse amplification (CPA) [9,10] technology has been utilized to achieve ultra-high-intensity pulse outputs in HPLSs. The laser-induced damage threshold (LIDT) of a multilayer dielectric grating (MLDG), which is a key optical component of the CPA system, directly determines the final output capacity of the entire system. Since MLDGs were proposed, the quest



https://doi.org/10.1017/hpl.2023.74 Published online by Cambridge University Press

for more robust MLDGs has promoted the investigation of their laser damage resistance enhancement and laser-induced damage mechanisms.

The first investigations on LIDT enhancement of MLDGs were reported in 1996 [11]. Although some benefits were obtained by optimizing the ion-beam etching manufacturing process [12], the electric-field intensity (EFI) enhancement introduced by the surface-relief grating structure was unavoidable, and the LIDT exhibited a strong dependence on the EFI. Because the initial damage of MLDGs induced by a ultrashort pulse is directly related to the EFI distribution [13,14], theoretical optimization of the near field in MLDGs has become the focus of several studies [13-16]. The EFI enhancement can be decreased by increasing the incident angle [12] and using a thin pillar profile [15]. Xie et al. [16] manufactured a rectangular MLDG profile to further reduce the EFI in the grating pillar. In addition, surface contaminants, including photoresists, etch residues, and surface debris, are well-known reasons for reducing the laser damage resistance [17-19]. Developing advanced cleaning methods, such as dilute-buffered hydrofluoric acid solution cleaning [20] and low-temperature chemical cleaning [21], can improve the laser damage resistance of MLDGs. Recently, these contaminants have been shown to extend to a 50- to 80-nm layer below the surface [22].

Efforts have been devoted to minimizing the peak EFI and reducing the subsurface contamination produced during MLDG fabrication [22,23]. However, potential defects, especially nodular defects in multilayer coating stacks [24], primarily limit the laser damage resistance of MLDGs exposed to nanosecond- and picosecond-laser irradiation [25-29]. Moreover, the presence of nodules results in the absence of a grating structure around the bulge area [30]. These factors necessitate the removal of nodular defects. Based on the successful application of laser conditioning in high reflectors and polarizers [31-38], we first propose removal of nodular defects in



https://doi.org/10.1017/hpl.2023.74 Published online by Cambridge University Press

MLDGs through nanosecond laser conditioning (NLC). Since the nodular defects are deposited during the preparation of multilayer dielectric films (MLDFs), the appropriate process stage for performing NLC needs to be identified. If NLC is performed before the surface-relief grating structure is fabricated (on the MLDF), then the pits and scalding regions induced by the MLDF conditioning may affect the subsequent lithography process. However, if the NLC is performed on the final grating products, can the effect of nodule removal on the surface-relief grating structure be tolerated?

In this study, two options for integrating NLC into the MLDG fabrication process were introduced to remove nodular defects. The NLC was applied to the MLDFs (Protocol 1) and final MLDGs (Protocol 2), as shown in Fig. 1 (b) and (c). We first investigated the effects of the nodular ejection pits formed in these two protocols and simulated their electric-field distributions using the finite element method (FEM). Subsequently, the morphological characteristics of the plasma-scalding regions that appeared in the two protocols were compared. Finally, nanosecond- and picosecond-laser raster scan damage tests were performed on the unconditioned and conditioned MLDGs to evaluate the overall effects of these two conditioning protocols. A maximum improvement of approximately 40 % was observed in the picosecond-LIDT of the MLDGs after the removal of the nodular defects.

## II. Sample and experimental protocols

MLDFs were deposited with alternating $HfO_2/SiO_2$ layers on a 50 mm × 50 mm × 1.5 mm fused silica substrate by electron beam evaporation. The basic stack formula [39] of the multilayer film is based on $(H2L)^k$, where H and L represent quarter-wave optical thickness layers of $HfO_2$ and $SiO_2$ respectively. Subsequently, the MLDFs were subjected to photoresist spin-coating, exposure, photoresist development, etching, and cleaning to obtain the final MLDGs. The MLDGs were designed with a groove density of 1740 lines/mm, which could provide a -1st-order diffraction



https://doi.org/10.1017/hpl.2023.74 Published online by Cambridge University Press

efficiency of more than 97 % at an incidence of 67° in a transverse electric (TE) polarized laser with a wavelength of 1064 nm [30].

The NLC process was introduced to the MLDF (Protocol 1) and final MLDG (Protocol 2), as shown in Fig. 1 (b) and (c), respectively. Subsequently, nanosecond- and picosecond-laser damage experiments were performed on the unconditioned and conditioned MLDGs to evaluate and compare their laser damage resistances. The raster scanning method [30] was applied in the NLC and laser damage experiments, and the distance between the neighboring test sites was equal to the diameter of the beam at 90 % of the peak fluence, as shown in Fig. 1 (d). The laser scanning speed was set to ~8.3 mm/s with a laser repetition rate of 30 Hz.

The NLC and nanosecond-laser experiments were performed using a 1064 nm Nd:YAG laser at an incidence of 67° in the TE polarization mode as described in [30]. The nanosecond-laser pulse width was ~8.0 ns, and the waist radius of the Gaussian beam at a normal incidence was ~0.6 mm. During the NLC process, the fluence of the incident laser was gradually increased from 12.8 to 28.4 J/cm$^2$, which was higher than that of the nanosecond-LIDTs of the samples. This was expected to remove nodular defects effectively and cause a negligible and benign damage.

The picosecond-laser damage apparatus is described in [40,41]. The incident laser was operated at a central wavelength of 1053 nm with an incident angle of 67° in the TE polarization mode. The picosecond-laser pulse width was ~8.6 ps, and the waist radius of the focused beam was ~ 48.9 μm. During the picosecond-laser damage experiment, the regions where the nodular defects and nodular ejection pits were generated by Protocols 1 and 2 were raster-scanned for comparison.

LIDT is defined as the maximum fluence at which no damage occurs. The laser fluence used in this study was provided as the beam normal. The damage density measured as a function of the



https://doi.org/10.1017/hpl.2023.74 Published online by Cambridge University Press

laser fluence was defined as the number of damage sites per scanning area (1 $cm^2$ for the raster scan in the final nanosecond-laser damage tests).

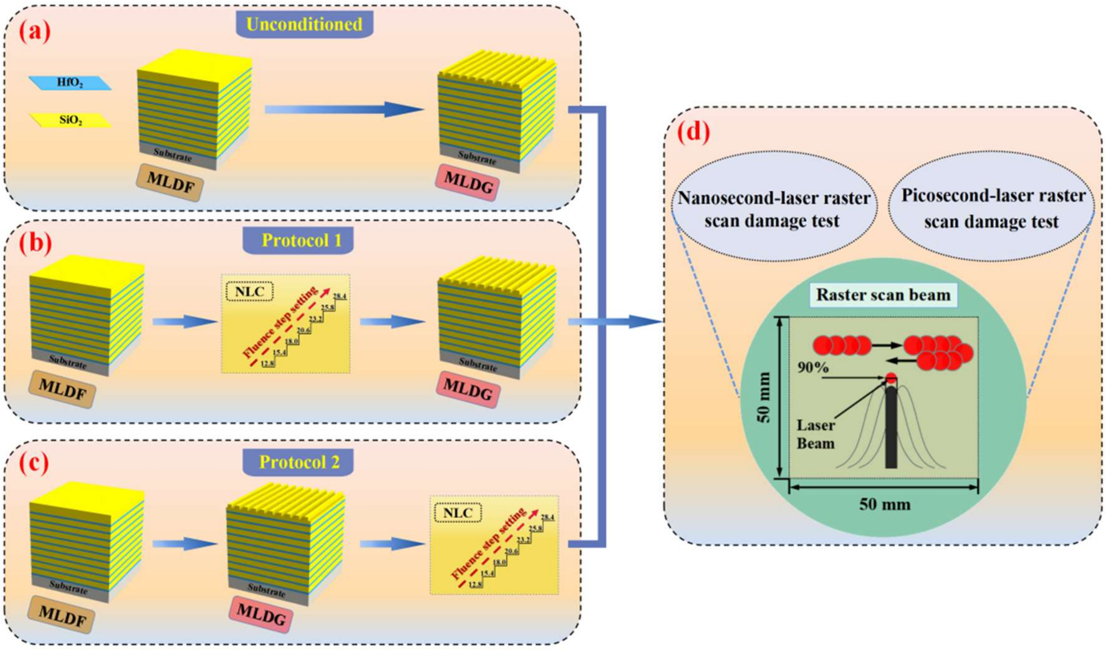


Fig. 1. Schematic representation of the nanosecond- and picosecond-laser damage tests performed on three types of MLDG samples: (a) Unconditioned MLDG, (b) MLDF conditioning, and (c) MLDG conditioning. (d) Schematic of the raster scan damage tests.

Optical microscopy (OM, Olympus BX53M) and focused ion beam scanning electron microscopy (FIB-SEM, Zeiss Auriga) were used to characterize the morphological evolution after conditioning, photoresist spin-coating, and cleaning in Protocol 1 as well as to evaluate the effects of the byproducts of the two protocols on the morphology of the grating surface. Finally, the laser damage resistance of the MLDGs conditioned by these two protocols were compared under a gradually increasing incident laser fluence.

## III. Morphological comparison and analysis

NLC with nodular defects introduced two typical byproducts (nodular ejection pits and plasma-scalding regions) in the final MLDGs. We first tracked the morphological characteristics of the



https://doi.org/10.1017/hpl.2023.74 Published online by Cambridge University Press

nodular ejection pits generated in Protocol 1 at different preparation stages. The effects of the two byproducts generated by these two protocols on the surface morphology of the MLDG were analyzed and compared.

### *3.1. Nodular ejection pits*

Fig. 2 shows the surface morphologies of the nodular ejection regions after the MLDF conditioning, spin-coating, and MLDG cleaning in Protocol 1. The nodular ejection pits marked as 1 and 3 in Fig. 2 (a) and (b), respectively, are accompanied by discolored plasma scalds, whereas the position marked as 2 in Fig. 2 (a) represents a nodular ejection pit without a scald. Fig. 2 (c)–(f) show that the nodular ejection pits and plasma scalds remain the same after the photoresist spin-coating and MLDG cleaning processes, respectively. Thus, the morphological modifications introduced by Protocol 1 exhibit replication characteristics at the subsequent process stages, and OM analyses reveal that these replication characteristics do not seem to affect the subsequent preparation process of the MLDG.

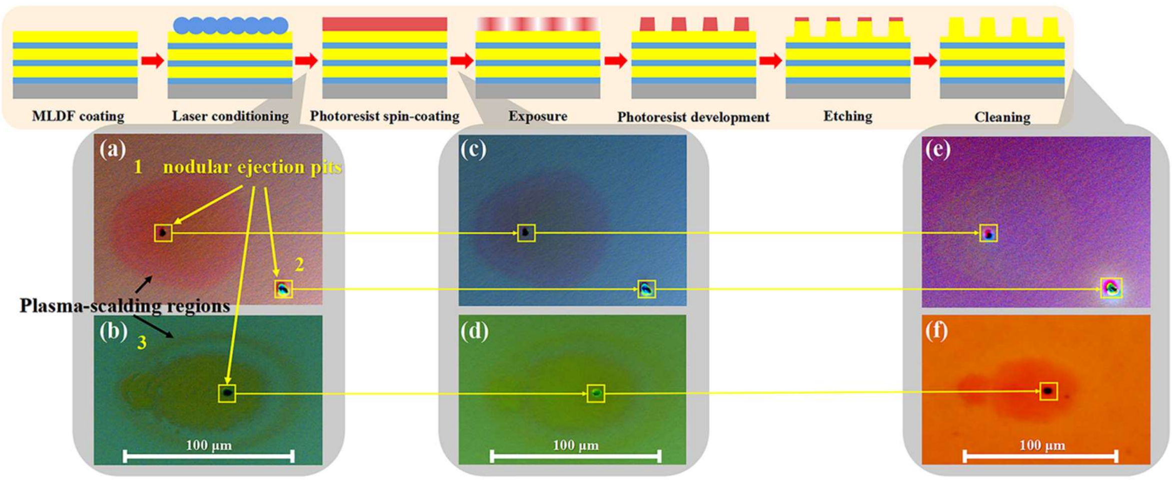


Fig. 2. OM images of the nodular ejection pits and plasma scalds originating from Protocol 1. (a) and (b) Before photoresist spin-coating after MLDF conditioning. (c) and (d) After photoresist spin-coating. (e) and (f) After MLDG cleaning.



https://doi.org/10.1017/hpl.2023.74 Published online by Cambridge University Press

Further morphological characterization was performed using SEM. Fig. 3 (a) shows the typical surface morphology of a nodular defect in the MLDF, which has an evident bulge structure. Fig. 3 (b)–(d) display the morphological characteristics corresponding to the nodular ejection pits after the MLDF conditioning, photoresist spin-coating, and MLDG cleaning, respectively. The results indicate that the pit is filled with photoresist after the spin-coating, and the multilayer structure in the pit cannot be observed, as shown in Fig. 3 (c). After cleaning, the internal structure of the pit was reproduced, and the grating relief structure was etched in the area around the pit, as shown in Fig. 3 (d).

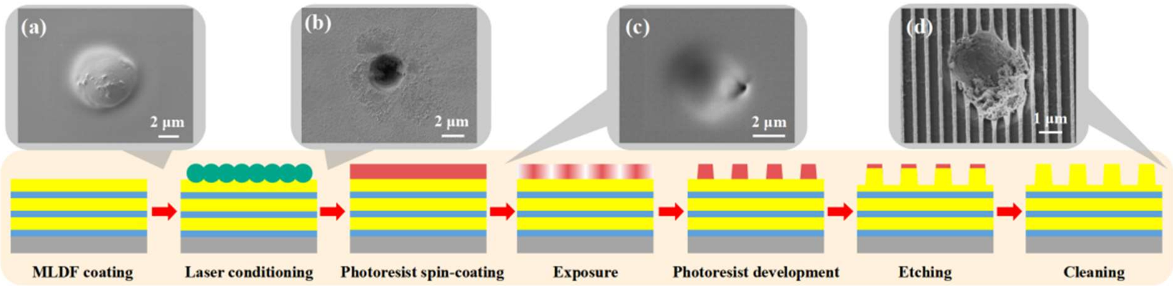


Fig. 3. SEM images of the nodular defect and ejection pits at the different MLDG fabrication stages. (a) Typical bulged nodular defect in the MLDF, and (b)–(d) morphologies of the nodular ejection pits after the MLDF conditioning, photoresist spin-coating, and grating cleaning, respectively.

The bulging nodular defect results in the absence of grating structures in the surrounding annular area, as shown in Fig. 3 (a), because of the presence of nodular defects, which affect the distribution of the surrounding exposure field during the exposure stage of the MLDG fabrication. After removing the nodule, as in Protocol 1, the nodular ejection pit in the MLDG exhibits a small affected area with a tightly surrounding grating structure, as shown in Fig. 4 (b). However, Protocol 2 cannot prevent the disappearance of grating structures around the nodular ejection pit, as shown in Fig. 4 (c). The square of EFI enhancement ($|E^2|$) distributions of the nodular defects and nodular ejection pits were simulated using the FEM. A two-dimensional simulation model with periodic boundaries on the left- and right-hand sides was used to reduce the computation. The simulation



https://doi.org/10.1017/hpl.2023.74 Published online by Cambridge University Press

domain was 100 μm wide and 7.5 μm high for nodular defects and nodular pits initiating from the 1 μm seeds. The geometry of the nodular defect can be expressed as: $D = sqrt(4dt)$ [42], where $D$ is the nodule diameter, $d$ is the diameter of the nodular seed, and $t$ is the seed depth. Table 1 lists the model parameters used in the calculations.

**Table 1. Model parameters used in the calculations.**

| Parameter | $d$ | $t$ | $n_L$ | $n_H$ | Wavelength | Incidence | Polarization |
|---|---|---|---|---|---|---|---|
| Value | 1 μm | 4.5 μm | 1.453 | 1.962 | 1064 nm | 67° | TE |

Note: $n_L$ and $n_H$ represent the refractive indices of $SiO_2$ and $HfO_2$, respectively.

The parabolic structure generated by the nodular ejection is reset as an air domain, and only the annular areas around the pits generated by Protocols 1 and 2 are different. Fig. 3 (d) shows the $|E^2|$ distributions of the bulged nodular defect, and Fig. 4 (e) and (f) depict the two typical nodular ejection pits caused by Protocols 1 and 2, respectively. The maximum $|E^2|$ of the nodular defect (= 5.5) is observed in the dome film at the top of the defect, as shown in Fig. 3 (d). In addition, a strong $|E^2|$ (= 3.7) is detected at the right boundary between the nodule and the holonomic layer. For the nodular ejection pits, the maximum $|E^2|$ in the pits generated by Protocols 1 and 2 decrease to 2.0 and 3.8, respectively, as shown in Fig. 3 (e) and (f). This result indicates that the laser damage resistance of the nodular ejection pits seems to be higher than that of the nodular defects, especially that of the pits generated in Protocol 1.



https://doi.org/10.1017/hpl.2023.74 Published online by Cambridge University Press

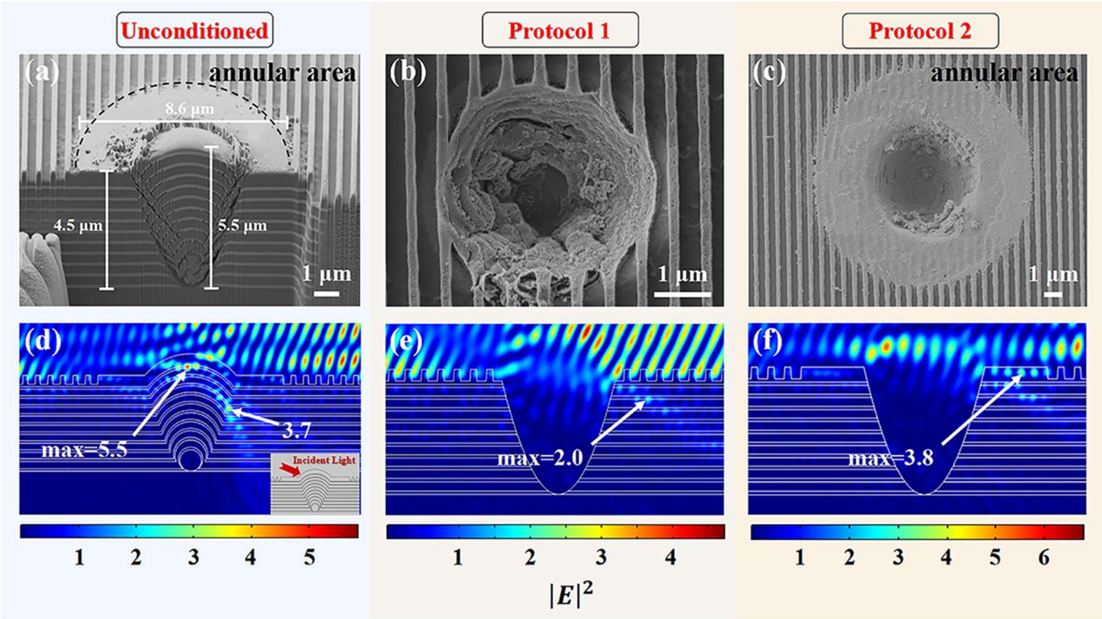


Fig. 4. (a) Typical cross-sectional morphology of a nodular defect in the unconditioned MLDG. (b) and (c) SEM images of the typical nodular ejection pits caused by Protocols 1 and 2, respectively. (d)–(f) Simulated $|E^2|$distributions corresponding to the morphological structures in (a)–(c), respectively.

*3.2. Plasma-scalding regions*

The effects of the plasma scalds, induced by the two protocols, on the final grating structure were evaluated. Fig. 5 (a) presents the typical morphology of a plasma-scalding region, with two elliptical structures and a bright nodular ejection pit, induced by Protocol 1. Six positions outside the center of the pit were selected for comparison. Fig. 55 (b)–(g) present the local magnified images of the positions marked by rectangles in Fig. 55 (a). For comparison, the pristine surface is also displayed in Fig. 55 (g), which shows a clear boundary between the pillars and grooves. In the elliptical plasma-scalding region, some molten holes are visible on the surface of the pillars, particularly at the edges of the two ellipses marked as c and e. In addition, the grating grooves, shown in Fig. 55 (c) and (e), exhibit some “wavy” features possibly due to the relatively severe scald; by contrast, this feature is not noticeable in the grating grooves at the positions marked as b



https://doi.org/10.1017/hpl.2023.74 Published online by Cambridge University Press

and d. At the outside point f, which is near the outer edge of the plasma-scalding region, the pillars and grooves are not affected, and the surface morphology is consistent with that of the primitive surface shown in Fig. 55 (g).

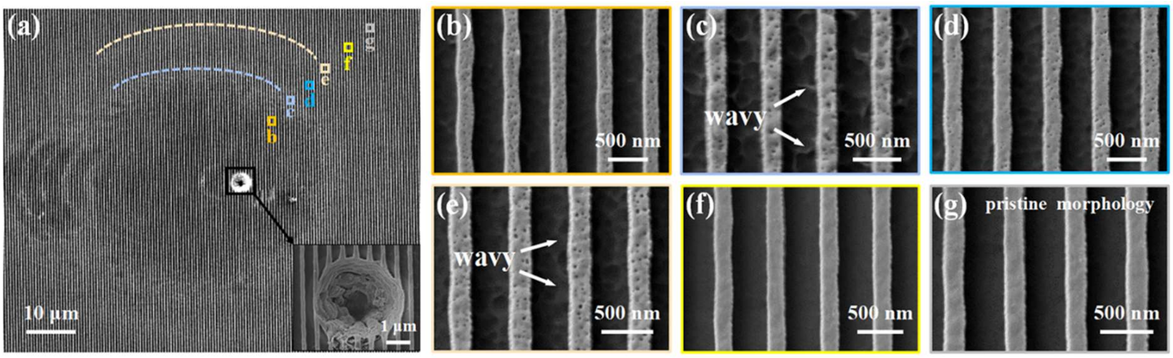


Fig. 5. (a) SEM image of the plasma-scalding region induced by the NLC in Protocol 1; the inset image shows a local magnified view of the nodular ejection pit. (b)−(g) Local magnified SEM images of the positions marked by rectangles (in color) in Fig. 55 (a).

The typical morphological characteristics of the bright plasma-scalding region with a nodular ejection pit induced by Protocol 2 are shown in Fig. 6 (a). Fig. 6 (b)–(g) show the local magnified SEM images of the six positions marked by rectangles (in color) in Fig. 6 (a). However, in contrast to the morphology induced by Protocol 1, in the case of Protocol 2, more molten holes are concentrated on the pillar surface, especially at the positions near the ejection pit marked by b and c. Furthermore, although many ejection residues also adhere to the surface of the grating pillars, the grating grooves are not modified, and their surfaces are smooth. At position f outside the scalding region, the morphological characteristics of the pillars are almost the same as those of the pristine surface of the MLDGs, as shown in Fig. 6 (f) and (g), similar to by Protocol 1.



https://doi.org/10.1017/hpl.2023.74 Published online by Cambridge University Press

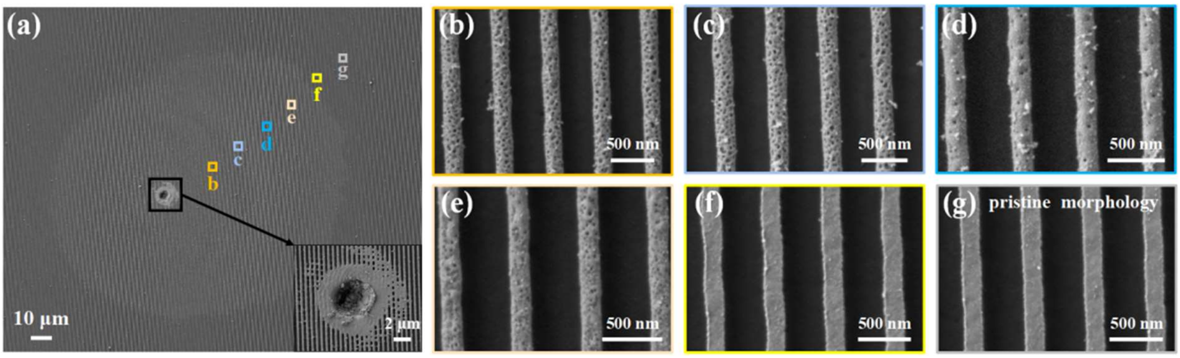


Fig. 6. (a) SEM image of the plasma-scalding region induced by the NLC in Protocol 2; the inset image indicates the local magnified view of the central nodular ejection pit. (b)−(g) Local magnified SEM images of the positions marked by rectangles (in color) in Fig. 56 (a).

# IV. Laser damage results and discussion

*4.1. Comparison of nanosecond-laser damage performances*

**4.1.1. LIDT and damage density**

The nanosecond-LIDTs and damage densities of the unconditioned and conditioned MLDGs are shown in **Error! Reference source not found.**7 (a) and (b), respectively. The LIDT of the MLDGs conditioned by Protocol 1 and that of the unconditioned MLDGs are almost the same (15.4 J/cm$^2$), whereas that of the MLDGs conditioned by Protocol 2 is higher (18.0 J/cm$^2$). The damage density is calculated as the number of damaged sites in an area of 1 cm$^2$. Overall, the damage densities of the three types of samples increase with the laser fluence for different slopes. The damage densities of the MLDGs conditioned using Protocols 1 and 2 decrease, especially that of the latter. Fig. 7 (b) shows that when the irradiated laser fluence reaches 25.8 J/cm$^2$, the damage density of the unconditioned MLDGs is 73 /cm$^2$, whereas those of the MLDGs conditioned by Protocols 1 and 2 are 50 and 3 /cm$^2$, respectively.



https://doi.org/10.1017/hpl.2023.74 Published online by Cambridge University Press

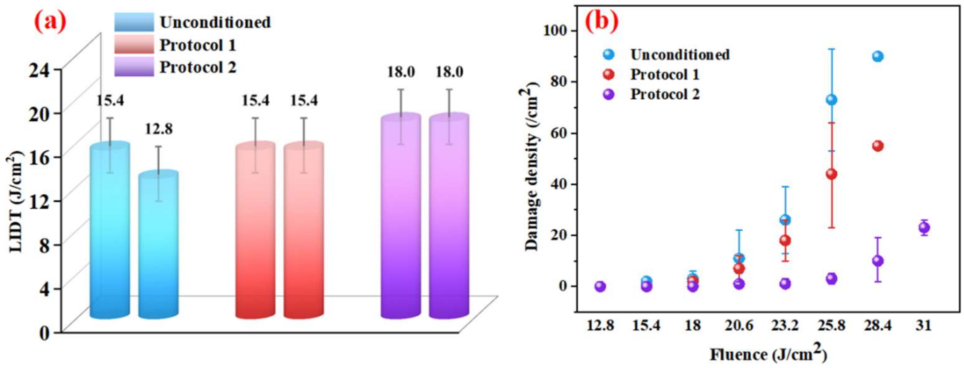


Fig. 7. (a) LIDT results of the nanosecond-laser raster scan, the two thresholds represent the results of two different test samples. (b) Damage density versus laser fluence (only the damage points that appear in the nanosecond-laser damage test process are counted as damage).

#### 4.1.2. Damage resistance of nodular ejection pits

The nanosecond-laser damage resistance of the nodular ejection pits induced by the two NLC protocols was further evaluated. Fig. 8 (a) shows the pristine morphological modifications of the three nodular ejection pits caused by the NLC in Protocol 1. The morphological evolution of the pits was characterized under gradually increasing incident laser fluence, and the corresponding results are shown in Fig. 8 (b)–(f). Even if new severely damaged modifications appear in the scanning area with no observable defects, the nodular ejection pit areas (marked by red lines) remain highly resistant to higher-fluence irradiation. This observation suggests that the nodular ejection pits induced by the NLC in Protocol 1 are stable and do not cause any catastrophic damage, even at a fluence of 38.8 J/cm$^2$, as shown in Fig. 8 (f).



https://doi.org/10.1017/hpl.2023.74 Published online by Cambridge University Press

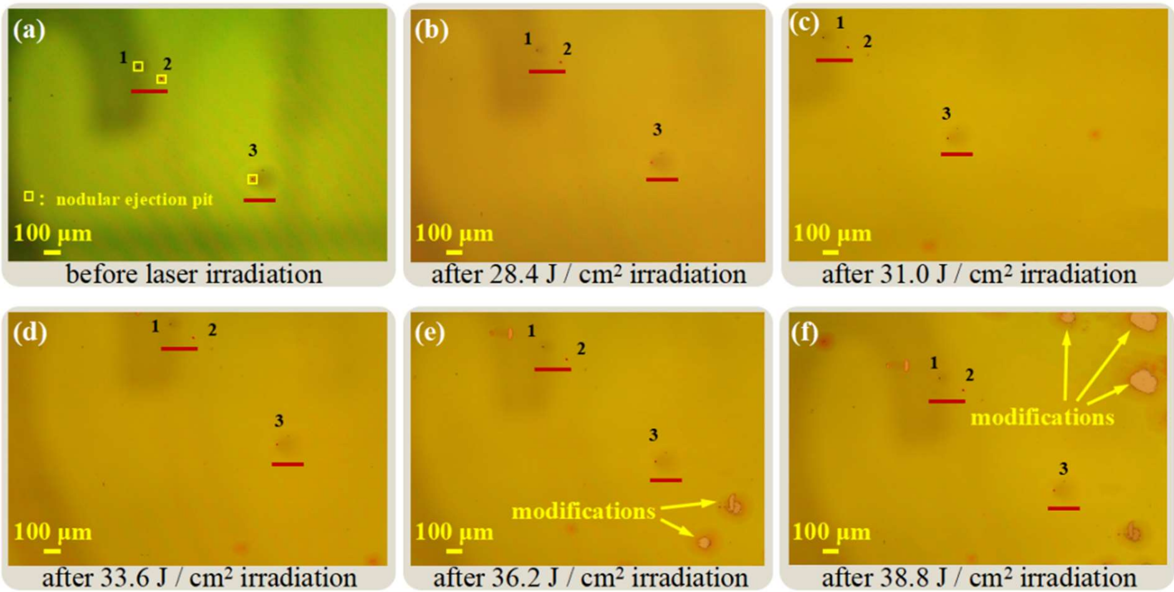


Fig. 8. (a) OM image showing the pristine morphological modifications of the three nodular ejection pits induced by the NLC in Protocol 1. (b)–(f) OM images showing the morphologies of the ejection pit areas irradiated by gradually increasing nanosecond-laser fluences; here, the red lines represent the nodular ejection pits on the MLDG.

The morphological changes in a nodular ejection pit caused by the NLC in Protocol 2 were also tracked under gradually increasing incident laser fluences, and the results are displayed in Fig. 9 (a) – (f). Similar to the pits in Protocol 1, the nodular ejection pit in Protocol 2 is highly stable under the irradiation of a laser fluence of 38.8 J/cm$^2$. When the laser fluence reaches 41.4 J/cm$^2$, noticeable modifications appear in the plasma-scalding area, as shown in Fig. 9 (f). Both the pits caused by the two NLC protocols can withstand a laser fluence of 38.8 J/cm$^2$, which is higher than twice the LIDTs of the unconditioned MLDGs (15.4 and 12.8 J/cm$^2$) shown in Fig. 7 (a).



https://doi.org/10.1017/hpl.2023.74 Published online by Cambridge University Press

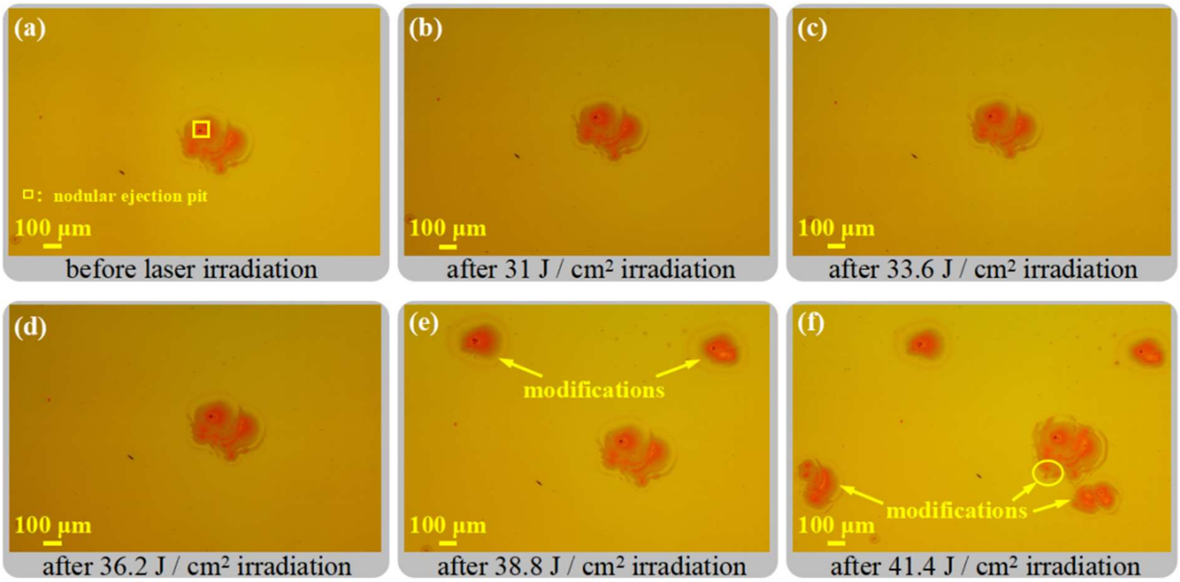


Fig. 9. (a) OM image showing the pristine morphological modifications of a nodular ejection pit induced by the NLC in Protocol 2. (b)–(f) Ejection pit region irradiated by gradually increasing nanosecond-laser fluences.

*4.2. Comparison of picosecond-laser damage performances*

**4.2.1. LIDT and damage morphology**

The picosecond-laser damage results of the nodular defects and nodular ejection pits caused by the NLC in Protocols 1 and 2 are displayed in Fig. 10. The LIDT of the nodular defects is 2.0 J/cm$^2$, which is the lowest among those of the three sites. The LIDTs for the areas of the nodular ejection pits produced by Protocols 1 and 2 are 2.8 and 2.2 J/cm$^2$, respectively, which are ~40 % and ~10 % higher than those of the nodular defects.

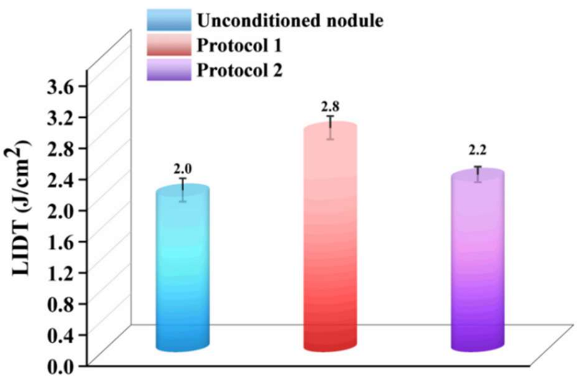




https://doi.org/10.1017/hpl.2023.74 Published online by Cambridge University Press

Fig. 10. Picosecond-LIDTs of the unconditioned nodule and nodular ejection pits conditioned by Protocols 1 and 2.

The nodular defects are partially or completely ejected under a low laser fluence of 2.0 J/cm$^2$, while the surrounding grating pillars remain intact, as shown in Fig. 11 (a) and (d). This result indicates that these unstable nodular defects limit the LIDT of the MLDG. Fig. 11 (b) and (e) show that the nodular ejection pit in Protocol 1 remains intact under a laser fluence of 2.4 J/cm$^2$ as well as remains stable under a laser fluence of 3.2 J/cm$^2$, while a catastrophic damage occurs in the surrounding pillars. The pillars near the ejection pit caused by Protocol 2 are more susceptible to damage than those caused by Protocol 1 and first fractured under a fluence of 2.2 J/cm$^2$, as shown in Fig. 11 (c). Fig. 11 (f) reveals that a laser fluence of 3.0 J/cm$^2$ damages almost all the pillars, and this damage may be attributed to the melting modification of the pillars in the plasma-scalding region, as shown in Fig. 6 (b) and (c).

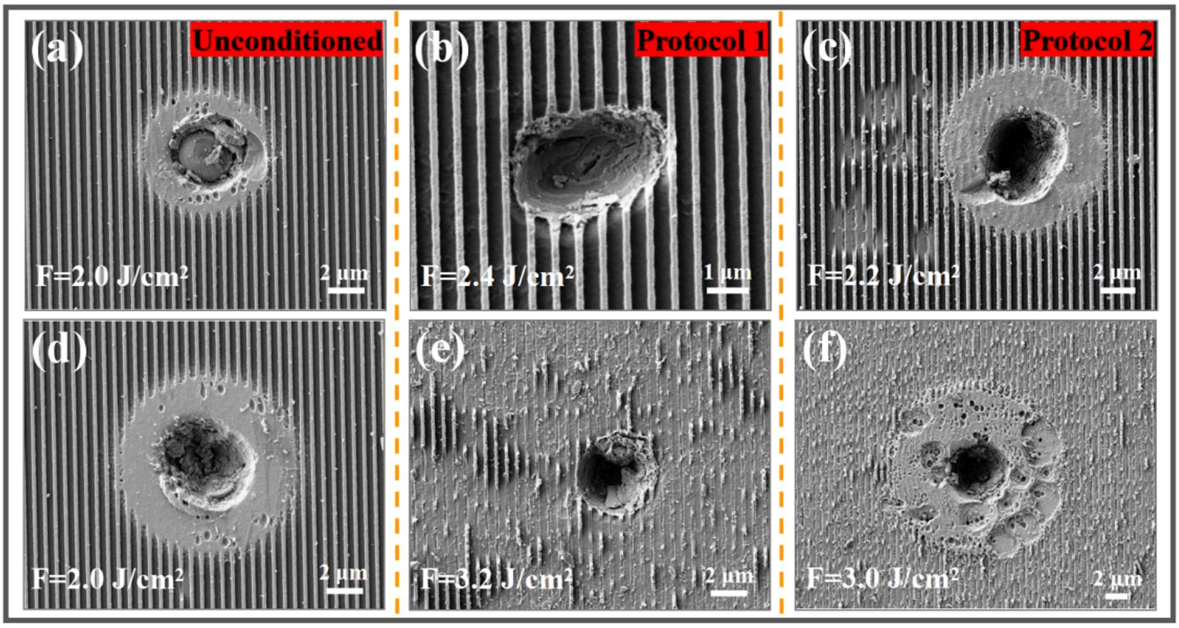


Fig. 11. Typical morphological characteristics of the different test areas induced during the picosecond-laser damage test. (a) and (d) Unconditioned nodular defects. (b) and (e) Nodular ejection pits caused by Protocol 1. (c) and (f) Nodular ejection pits caused by Protocol 2 (where F denotes the incident laser fluence).

#### 4.2.2. Damage resistance of nodular ejection pits



https://doi.org/10.1017/hpl.2023.74 Published online by Cambridge University Press

The picosecond-laser damage resistance of the two types of nodular ejection pits was evaluated by gradually increasing the laser fluence. Fig. 12 (b) – (f) show the morphological evolution of the nodular ejection pit in the case of Protocol 1. When the laser fluence is 2.8 J/cm$^2$, the damage first occurs in the grating pillar area near the ejection pit, as shown in Fig. 12 (e). As the laser fluence increases to 3.0 J/cm$^2$, the initial damaged area surrounding the ejection pit expands further; however, the ejection pit remains stable, as shown in Fig. 12 (f).

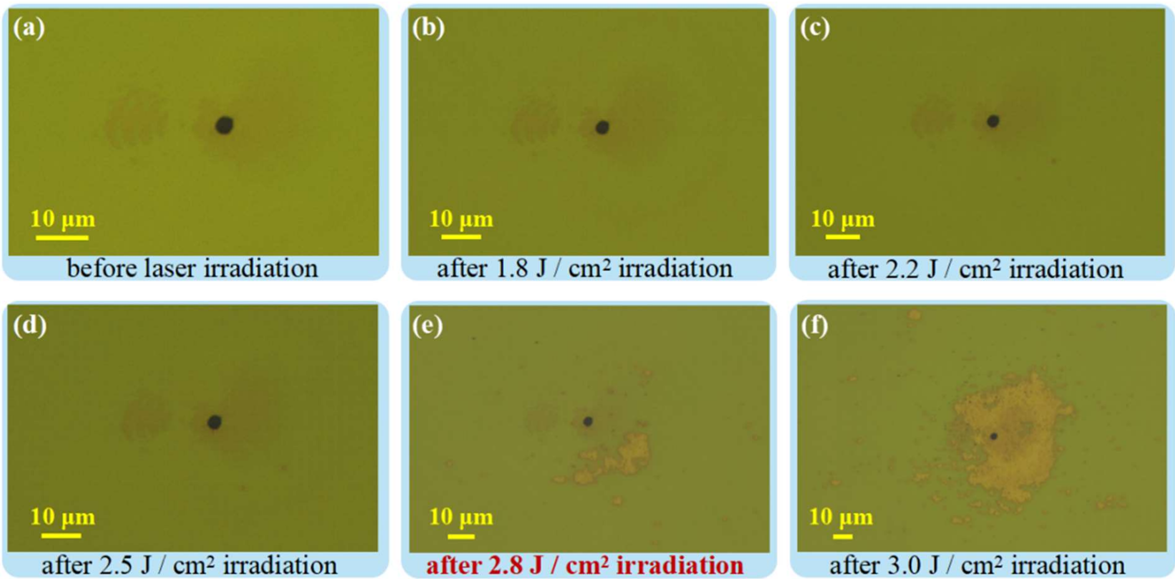


Fig. 12. (a) OM image showing the pristine morphological modification of a nodular ejection pit in Protocol 1. (b)–(f) OM images showing the morphologies of the ejection pit area irradiated by gradually increasing the picosecond-laser fluences.

Fig. 13 (a) shows an OM image of a pristine nodular ejection pit with an annular plasma-scalding area caused by Protocol 2. The morphological evolution of the pit irradiated by gradually increasing the picosecond-laser fluence is shown in Fig. 13 (b) – (f). Evidently, the damage first occurs in the plasma-scalding region on the left side of the ejection pit at a low laser fluence of 2.2 J/cm$^2$, as shown in Fig. 13 (c). As the incident laser fluence is increased, the damaged area gradually expands. When the laser fluence reaches 3.0 J/cm$^2$, almost the entire



https://doi.org/10.1017/hpl.2023.74 Published online by Cambridge University Press

plasma-scalding region is catastrophically damaged, which may be caused by a more serious modification of the region during the NLC process.

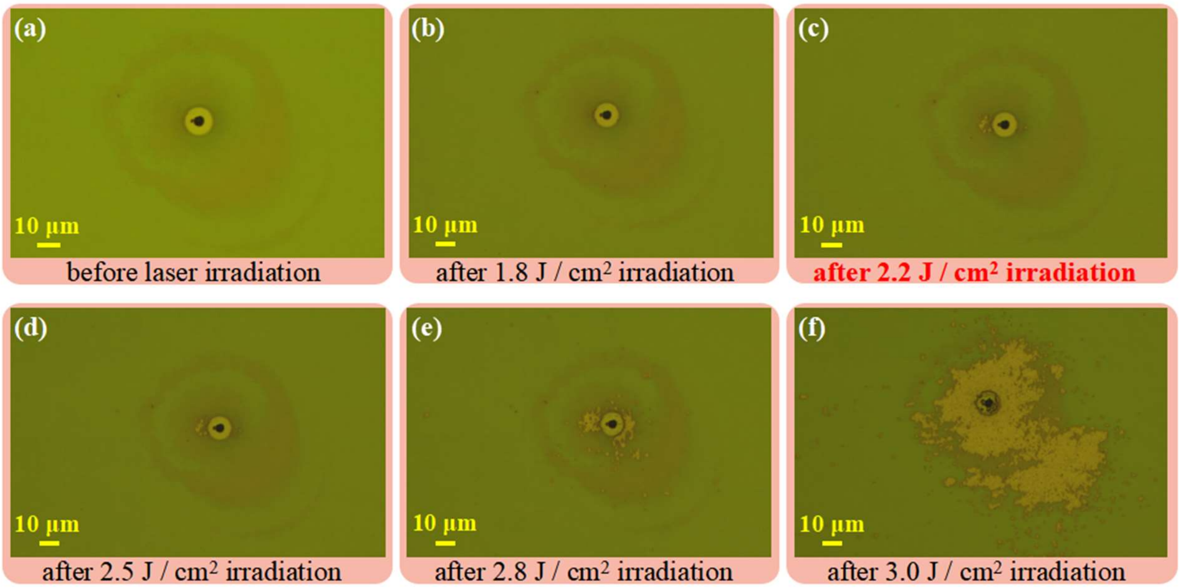


Fig. 13. (a) OM image showing the pristine morphological modification of a nodular ejection pit in Protocol 2. (b)–(f) OM images showing the morphologies of the ejection pit area irradiated by gradually increasing picosecond-laser fluences.

## V. Conclusion

In this study, NLC, an effective method for removing nodular defects, was integrated into the different MLDG fabrication stages, i.e., after the MLDF coating (Protocol 1) and cleaning (Protocol 2). Subsequently, nanosecond- and picosecond-laser raster scan damage tests were performed on the unconditioned and conditioned MLDGs for comparison.

Following the MLDF conditioning, the modifications caused by the nodular ejection pit and plasma scald exhibited morphological replication after the photoresist spin-coating and cleaning of the MLDG. Unlike bulging nodular defects, the ejection pits did not eliminate the surrounding grating structure. In addition, the remaining nodular ejection pits introduced by the two protocols



https://doi.org/10.1017/hpl.2023.74 Published online by Cambridge University Press

exhibited a high nanosecond-laser stability and remained stable even when the irradiated laser fluence was more than twice the nanosecond-LIDTs of the unconditioned MLDGs. The picosecond-LIDT of the nodular ejection pits produced by the MLDF conditioning was ~40 % higher than that of the nodular defects, whereas the LIDT of the nodular ejection pit produced by the MLDG conditioning increased by only ~10 % owing to the melting modification of the plasma-scalding region around the pit during the NLC process. Both the protocols can remove nodular defects to improve the laser damage performance of MLDGs.

Laser conditioning performed using nanosecond pulses are universal and can be easily integrated, because a vacuum environment to prevent the nonlinear self-focusing in air, which occurs under the picosecond regime, is not required. Consequently, the NLC can be applied to large-aperture gratings to improve their laser damage resistance.

## Acknowledgments

This research was supported by the National Key R&D Program of China (2018YFE0115900), the Key Foreign Cooperation Projects of Bureau of International Cooperation of Chinese Academy of Sciences (Grant No. 181231KYSB20210001), and the Strategic Priority Research Program of Chinese Academy of Sciences (Grant No.XDA25020314). The authors would like to express their gratitude to Yun Cui, Jialong Gu, Lili Liu, Ziyuan Xu and Fanyu Kong from the Shanghai Institute of Optics and Fine Mechanics for their help with the SEM observation, laser-induced damage tests and grating preparation.

## References

1. M. D. Perry, D. Pennington, B. C. Stuart, G. Tietbohl, J. A. Britten, C. Brown, S. Herman, B. Golick, M. Kartz, J. Miller, H. T. Powell, M. Vergino, and V. Yanovsky, "Petawatt laser pulses," Opt. Lett. 24(3), 160-162 (1999).



https://doi.org/10.1017/hpl.2023.74 Published online by Cambridge University Press

2. L. J. Waxer, D. N. Maywar, J. H. Kelly, T. J. Kessler, B. E. Kruschwitz, S. J. Loucks, R. L. McCrory, D. D. Meyerhofer, S. F. B. Morse, C. Stoeckl, and J. D. Zuegel, “High-energy petawatt capability for the OMEGA laser,” Opt. Photonics News 16(7), 30-36 (2005).
3. C. Radier, O. Chalus, M. Charbonneau, S. Thambirajah, G. Deschamps, S. David, J. Barbe, E. Etter, G. Matras, S. Ricaud, V. Leroux, C. Richards, F. Lureau, A. Baleanu, R. Banici, A. Gradinariu, C. Caldararu, C. Capiteanu, A. Naziru, B. Diaconescu, V. Iancu, R. Dabu, D. Ursescu, I. Dancus, C. A. Ur, K. A. Tanaka, and N. V. Zamfir, “10 PW peak power femtosecond laser pulses at ELI-NP,” High Power Laser Sci. Eng. 10(3), e21 (2022).
4. N. Blanchot, G. Behar, T. Berthier, B. Busserole, C. Chappuis, C. Damiens-Dupont, P. Garcia, F. Granet, C. Grosset-Grange, J. P. Goossens, L. Hilsz, F. Laborde, T. Lacombe, F. Laniesse, E. Lavastre, J. Luce, F. Macias, E. Mazataud, J. L. Miquel, J. Neauport, S. Noailles, P. Patelli, E. Perrot-Minot, C. Present, D. Raffestin, B. Remy, C. Rouyer, and D. Valla, “Overview of PETAL, the multi-Petawatt project in the LMJ facility,” in Eighth-International-Conference-on-Inertial-Fusion-Sciences-and-Applications (IFSA, 2011), paper 07001 (2013).
5. R. Tommasini, O. L. Landen, L. B. Hopkins, S. P. Hatchett, D. H. Kalantar, W. W. Hsing, D. A. Alessi, S. L. Ayers, S. D. Bhandarkar, M. W. Bowers, D. K. Bradley, A. D. Conder, J. M. Di Nicola, P. Di Nicola, L. Divol, D. Fittinghoff, G. Gururangan, G. N. Hall, M. Hamamoto, D. R. Hargrove, E. P. Hartouni, J. E. Heebner, S. I. Herriot, M. R. Hermann, J. P. Holder, D. M. Holunga, D. Homoelle, C. A. Iglesias, N. Izumi, A. J. Kemp, T. Kohut, J. J. Kroll, K. LaFortune, J. K. Lawson, R. Lowe-Webb, A. J. MacKinnon, D. Martinez, N. D. Masters, M. P. Mauldin, J. Milovich, A. Nikroo, J. K. Okui, J. Park, M. Prantil, L. J. Pelz, M. Schoff, R. Sigurdsson, P. L. Volegov, S. Vonhof, T. L. Zobrist, R. J. Wallace, C. F. Walters, P. Wegner, C. Widmayer, W. H. Williams, K. Youngblood, M. J. Edwards, and M. C. Herrmann, “Time-resolved fuel density profiles of the stagnation phase of indirect-drive inertial confinement implosions,” Phys. Rev. Lett. 125(15), (2020).
6. S. P. Hatchett, C. G. Brown, T. E. Cowan, E. A. Henry, J. S. Johnson, M. H. Key, J. A. Koch, A. B. Langdon, B. F. Lasinski, R. W. Lee, A. J. Mackinnon, D. M. Pennington, M. D. Perry, T. W. Phillips, M. Roth, T. C. Sangster, M. S. Singh, R. A. Snavely, M. A. Stoyer, S. C. Wilks, and K. Yasuike, “Electron, photon, and ion beams from the relativistic



https://doi.org/10.1017/hpl.2023.74 Published online by Cambridge University Press

interaction of Petawatt laser pulses with solid targets," Phys. Plasmas 7(5), 2076-2082 (2000).

7. A. X. Li, C. Y. Qin, H. Zhang, S. Li, L. L. Fan, Q. S. Wang, T. J. Xu, N. W. Wang, L. H. Yu, Y. Xu, Y. Q. Liu, C. Wang, X. L. Wang, Z. X. Zhang, X. Y. Liu, P. L. Bai, Z. B. Gan, X. B. Zhang, X. B. Wang, C. Fan, Y. J. Sun, Y. H. Tang, B. Yao, X. Y. Liang, Y. X. Leng, B. F. Shen, L. L. Ji, R. X. Li, and Z. Z. Xu, "Acceleration of 60 MeV proton beams in the commissioning experiment of the SULF-10 PW laser," High Power Laser Sci. Eng. 10(4), e26 (2022).
8. H. Daido, M. Nishiuchi, and A. S. Pirozhkov, "Review of laser-driven ion sources and their applications," Rep. Prog. Phys. 75(5), 056401 (2012).
9. D. Strickland and G. Mourou, "Compression of amplified chirped optical pulses," Opt. Commun. 56(3), 219–221(1985).
10. Z. Chen, S. Zheng, X. Lu, X. Wang, Y. Cai, C. Wang, M. Zheng, Y. Ai, Y. Leng, S. Xu, and D. Fan, "Forty-five terawatt vortex ultrashort laser pulses from a chirped-pulse amplification system," High Power Laser Sci. Eng. 10(5), e32 (2022).
11. B. C. Stuart, M. D. Feit, S. Herman, et al., "Optical ablation by high-power short-pulse lasers," J Opt Soc Am B 13, 459-468 (1996).
12. J. A. Britten, W. A. Molander, A. M. Komashko, et al., "Multilayer dielectric gratings for petawatt-class laser systems," Proc. SPIE 5273, 1-7 (2004).
13. J. Neauport, E. Lavastre, G. Razé, G. Dupuy, and F. Desserouer, "Effect of electric field on laser induced damage threshold of multilayer dielectric gratings," Opt. Express 15(19), 12508-12522 (2007).
14. N. Bonod and J. Néauport, "Optical performance and laser induced damage threshold improvement of diffraction gratings used as compressors in ultra high intensity lasers," Opt. Commun. 260(2), 649–655 (2006).
15. J. Néauport, and N. Bonod, "Pulse compression gratings for the PETAL project: a review of various technologies," Proc. SPIE 7132, 71320D (2009).
16. L. Y. Xie, J. L. Zhang, Z. Y. Zhang, B. Ma, and X. B. Cheng, "Rectangular multilayer dielectric gratings with broadband high diffraction efficiency and enhanced laser damage resistance," Opt. Express 29(2), 2669-2678 (2021).



https://doi.org/10.1017/hpl.2023.74 Published online by Cambridge University Press

17. B. Ashe, K. L. Marshall, C. Giacofei, A. L. Rigatti, T. J. Kessler, A. W. Schmid, J. B. Oliver, J. Keck, and A. Kozlov, “Evaluation of cleaning methods for multilayer diffraction gratings,” Proc. SPIE 6403, 64030O (2006).

18. B. Ashe, K. L. Marshall, D. Mastrosimone, and C. McAtee, “Minimizing contamination to multilayer dielectric diffraction gratings within a large vacuum system,” Proc. SPIE 7069, 706902 (2008).

19. B. Ashe, C. Giacofei, G. Myhre, and A. W. Schmid, “Optimizing a cleaning process for multilayer-dielectric- (MLD) diffraction gratings,” Proc. SPIE 6720, 67200N (2007).

20. H. T. Nguyen, C. C. Larson, and J. A. Britten, “Improvement of laser damage resistance and diffraction efficiency of multilayer dielectric diffraction gratings by HF etchback linewidth tailoring,” Proc. SPIE 7842, 78421H (2010).

21. H. P. Howard, A. F. Aiello, J. G. Dressler, N. R. Edwards, T. J. Kessler, A. A. Kozlov, I. Manwaring, K. L. Marshall, J. B. Oliver, and S. Papernov, “Improving the performance of high-laser-damage-threshold, multilayer dielectric pulse-compression gratings through low-temperature chemical cleaning,” Appl. Opt. 52(8), 1682-1692 (2013).

22. N. Liu, R. Dent, B. N. Hoffman, A. A. Kozlov, J. B. Oliver, A. L. Rigatti, T. J. Kessler, S. G. Demos, and A. A. Shestopalov, "Manufacturing- induced contamination in common multilayerdielectric gratings," Opt. Express 31(1), 714-726 (2023).

23. J. Néauport, N. Bonod, and S. Hocquet, “Recent progress in the development of pulse compression gratings,” Proc. SPIE 8190, 81900O (2011).

24. T. Liu, M. Zhu, W. Du, J. Shi, J. Sun, Y. Chai, and J. Shao, “A nodule dome removal strategy to improve the laser-induced damage threshold of coatings,” High Power Laser Sci. Eng. 10(5), e30 (2022).

25. X. Zou, F. Y. Kong, Y. X. Jin, P. Chen, J. M. Chen, J. Xu, Y. L. Wang, Y. B. Zhang, and J. D. Shao, “Influence of nodular defect size on metal dielectric mixed gratings for ultra-short ultra-high intensity laser system,” Opt. Mater. 91, 177-182 (2019).

26. D. A. Alessi, C. W. Carr, R. P. Hackel, R. A. Negres, K. Stanion, J. E. Fair, D. A. Cross, J. Nissen, R. Luthi, G. Guss, J. A. Britten, W. H. Gourdin, and C. Haefner, “Picosecond laser damage performance assessment of multilayer dielectric gratings in vacuum,” Opt. Express 23(12), 15532-15544 (2015).

27. J. Xu, X. Zou, J. M. Chen, Y. B. Zhang, Y. L. Wang, Y. X. Jin, F. Y. Kong, H. C. Cao, P. Chen, and J. D. Shao, “Metal dielectric gratings with high femtosecond laser damage threshold of twice as much as that of traditional gold gratings,” Opt. Lett. 44, 2871-2874 (2019).

28. H. Liddell, “Enhancing the performance of multilayer-dielectric diffraction gratings through cleaning process modifications and defect mitigation,” PhD. Thesis (University of Rochester, 2014).

29. I. Jovanovic, C. G. Brown, B. C. Stuart, et al., “Precision damage tests of multilayer dielectric gratings for high-energy petawatt lasers,” Proc. SPIE 5647, 34-42 (2005).

30. X. K. Lin, Y. A. Zhao, X. F. Liu, D. W. Li, K. Shuai, H. Ma, Y. C. Shao, J. Sun, K. Q. Qiu, Y. Cui, Y. P. Dai, and J. D. Shao, “Damage characteristics of pulse compression grating irradiated by nanosecond laser,” Opt. Mater. Express 12(2), 643-652 (2022).

31. S. Xu, X. Yuan, Y. Wei, X. Xia, and X. Zu, “Effect of UV laser conditioning on fused silica in vacuum,” Opt. Mater. 31, 1013-1016 (2009).

32. M. Sahraee, H. R. Fallah, H. Zabolian, B. Moradi, and M. H. Mahmoodzade, “Influence of laser conditioning on laser induced damage threshold of single layers of ZrO 2 with various deposition conditions,” Opt. Spectrosc+. 118, 627-630 (2015).

33. C. J. Stolz, L. M. Sheehan, S. M. Maricle, S. Schwartz, M. R. Kozlowski, R. T. Jennings, and J. Hue, “Laser conditioning methods in hafnia silica multilayer mirrors,” Proc. SPIE 3264, 105–112 (1998).

34. M. Kozlowski, C. Wolfe, M. Staggs, and J. Campbell, “Large area laser conditioning of dielectric thin film mirrors,” Proc. SPIE 1438, 143811 (1998).

35. H. Bercegol, “What is laser conditioning: a review focused on dielectric multilayers,” Proc. SPIE 3578, 421–426 (1998).

36. Y. N. Zhao, T. Wang, D. W. Zhang, J. Shao, and Z. Fan, “Laser conditioning and multi-shot laser damage accumulation effects of HfO2/SiO2 antireflective coatings,” Appl. Surf. Sci. 245(1-4), 335–339 (2005).

37. J. Liu, X. Li, Z. K. Yu, H. Cui, W. L. Zhang, M. P. Zhu, and K. Yi, “Effect of laser conditioning on the LIDT of 532nm HfO2/SiO2 thin films reflectors,” Proc. SPIE 8786, 87860Z (2013).



https://doi.org/10.1017/hpl.2023.74 Published online by Cambridge University Press

38. Y. Zhao, J. Shao, T. Wang, D. Zhang, S. Fan, J. Huang, W. Gao, and Z. Fan, “Laser conditioning of dielectric oxide mirror coatings at 1064 nm,” Proc. SPIE 5774, 599–602 (2004).
39. X. K. Lin, Y. A. Zhao, X. F. Liu, D. W. Li, H. Ma, Y. C. Shao, K. Q. Qiu, J. Sun, F. Y. Kong, M. P. Zhu, and J. D. Shao, “Nanosecond laser damage characteristics of multilayer dielectric films and gratings,” Proc. SPIE 11912, 119120O (2021).
40. Y. Hao, M. Sun, S. Shi, X. Pan, Z. Zhu, X. Pang, and J. Zhu, “Comparison between intrinsic and contaminant-induced damages of multilayer dielectric gratings,” Proc. SPIE 10339, 103390H (2017).
41. K. Shuai, X. Liu, Y. Zhao, K. Qiu, D. Li, H. Gong, J. Sun, L. Zhou, Y. Jiang, Y. Dai, J. Shao, Z. Xia. “Multilayer dielectric grating pillar-removal damage induced by a picosecond laser,” High Power Laser Sci. Eng. 10(6), e42 (2022).
42. X. Cheng, J. Zhang, T. Ding, Z. Wei, H. Li, and Z. Wang, “The effect of an electric field on the thermomechanical damage of nodular defects in dielectric multilayer coatings irradiated by nanosecond laser pulses,” Light-Sci. Appl. 2, e80 (2013).




https://doi.org/10.1017/hpl.2023.74 Published online by Cambridge University Press